

# The 2019 Ridgecrest, California, Earthquake Sequence Ground Motions: Processed Records and Derived Intensity Metrics

John M. Rekoske<sup>1</sup>, Eric M. Thompson<sup>\*1</sup>, Morgan P. Moschetti<sup>1</sup>, Mike G. Hearne<sup>1</sup>, Brad T. Aagaard<sup>1</sup>, and Grace A. Parker<sup>2</sup>

## Abstract

Following the 2019 Ridgecrest, California, earthquake sequence, we compiled ground-motion records from multiple data centers and processed these records using newly developed ground-motion processing software that performs quality assurance checks, performs standard time series processing steps, and computes a wide range of ground-motion metrics. In addition, we compute station and waveform metrics such as the time-averaged shear-wave velocity to 30 m depth ( $V_{s30}$ ), finite-rupture distances, and spectral accelerations. This data set includes 22,708 records from 133 events from 4 July 2019 (UTC) to 18 October 2019 with a magnitude range from 3.6 to 7.1. We expect that the rapid collection and dissemination of this information will facilitate detailed studies of these ground motions. In this article, we describe the data selection, processing steps, and how to access the data.

**Cite this article as** Rekoske, J. M., E. M. Thompson, M. P. Moschetti, M. G. Hearne, B. T. Aagaard, and G. A. Parker (2020). The 2019 Ridgecrest, California, Earthquake Sequence Ground Motions: Processed Records and Derived Intensity Metrics, *Seismol. Res. Lett.* **XX**, 1–14, doi: [10.1785/0220190292](https://doi.org/10.1785/0220190292).

## Introduction

The 2019 Ridgecrest, California, earthquake sequence included the largest earthquake to occur in southern California in about 20 yr, and the station density has increased significantly over this time period. As a result, this earthquake sequence is one of the best-recorded earthquakes in California, making it particularly useful for understanding ground motions from shallow strike-slip earthquakes. The purpose of this article is to rapidly provide the ground motions in a uniformly processed manner, along with commonly used ground-motion and station metrics.

Ground-motion records and their derived metrics have proven to be extremely valuable to the engineering seismology community and U.S. Geological Survey (USGS) products such as the National Seismic Hazard Model (NSHM; Petersen *et al.*, 2015) and ShakeMap (Worden and Wald, 2016). The ground-motion data compiled in this article are derived from both permanently installed instruments and temporary deployments. The aftershock response by the USGS is described in more detail by Cochran *et al.* (2019). The data set described in this article includes 22,708 records from 133 earthquakes, from 986 stations, maintained by 18 different networks. We use open-source ground-motion processing software in Python called gmprocess (Hearne *et al.*, 2019) to retrieve the time-series data, process the records, and compute derived ground-motion intensity measures.

The retrieval of event-based records, their metadata, and the processing of the records is a routine but cumbersome task

and has traditionally required manual review of each record. Providing the processed data quickly, in a public repository committed to long-term maintenance, and in a well-documented format facilitates consistency and transparency and avoids duplicative efforts. For example, the Next Generation Attenuation-West1 Project (Chiou *et al.*, 2008) provided a data set of spectral accelerations (SAs) for active crustal earthquakes that has been extensively used by both researchers and practicing engineers. The Next Generation Attenuation-West2 Project (Ancheta *et al.*, 2014) expanded this data set to include many more records spanning a wider range of magnitudes and was used to develop a new set of ground-motion models (Gregor *et al.*, 2014) that are used in the USGS NSHM. An analogous effort in Europe by Akkar *et al.* (2014) developed a database of ground motions and derived metrics, referred to as the Reference Database for Seismic Ground Motion in Europe database. More recently, Luzzi *et al.* (2016) created the European Engineering Strong Motion (ESM) database, which is continuously updated with new waveforms throughout Europe; the ESM database is the basis for the flat file of derived waveforms and metadata developed by Lanzano *et al.* (2019). These valuable

1. U.S. Geological Survey, Denver Federal Center, Denver, Colorado, U.S.A.; 2. U.S. Geological Survey, Moffett Field, California, U.S.A.

\*Corresponding author: [emthompson@usgs.gov](mailto:emthompson@usgs.gov)

© Seismological Society of America

data sets have required a massive investment of time and resources to process the ground motions, ensure consistency and accuracy (e.g., [Bindi et al., 2019](#)), and distribute the data through a user-friendly interface in a timely manner.

The value of these data products, along with expanded network coverage, has motivated efforts on automated or semiautomated ground-motion processing methods. For example, [Dawood et al. \(2016\)](#) produced a database of waveform metrics for records from KiK-net, along with compiled station and event metadata, including the classification of event tectonic regime based on the [García, Wald, and Hearne \(2012\)](#) method. Similarly, [Rennolet et al. \(2018\)](#) produced a ground-motion database for induced earthquakes in Oklahoma and Kansas using automated processing techniques, which was used by [McNamara et al. \(2018\)](#) and [Moschetti et al. \(2019\)](#) for ground-motion analysis. The need for software and standardized methods to facilitate ground-motion data collection and processing has recently received more attention. For example, [Cauzzi et al. \(2016\)](#) developed the European Rapid Raw Strong-Motion database that uses automated processing routines in the open-source SeisComP3 software (see [Data and Resources](#)) to produce a database of ground-motion metrics in near-real time. [Puglia et al. \(2018\)](#) developed a webservice that is integrated with the ESM and provides interactive processing functionality. [Zaccarelli et al. \(2019\)](#) developed software that facilitates event-based ground-motion data retrieval, visualization, and processing. [Jones et al. \(2017\)](#) developed the processing and review interface for strong-motion data software for automatically processing strong-motion data that is currently used for processing records at the California Geological Survey and the USGS National Strong Motion Program.

In parallel with these efforts, [Hearne et al. \(2019\)](#) developed open-source ground-motion processing software in Python called gmprocess to fulfill the specific needs of the USGS near-real-time earthquake response program. The gmprocess code relies heavily on the ObsPy Python library ([Krischer, Megies, et al., 2015](#)) for processing seismological data. At the USGS, we primarily use this software for collecting and processing historical data for the ShakeMap Atlas ([García, Mah, et al., 2012](#)) as well as current events located outside of the United States. Additional applications include analyses of regionalized ground-motion features and evaluation of existing ground-motion models for seismic hazard assessments (e.g., [McNamara et al., 2019](#); [Moschetti et al., 2019](#)). The gmprocess software facilitates automated retrieval from a wide variety of data providers and readers for all of the file formats that we have encountered. For events within the United States, the software collects records from data centers that provide Federation of Digital Seismograph Networks (FDSN) webservices such as the Southern California Seismic Network (SCSN), Northern California Seismic Network (NCSN), and the Incorporated Research Institutions for Seismology (IRIS). Some ground-motion data are only distributed through the Center for

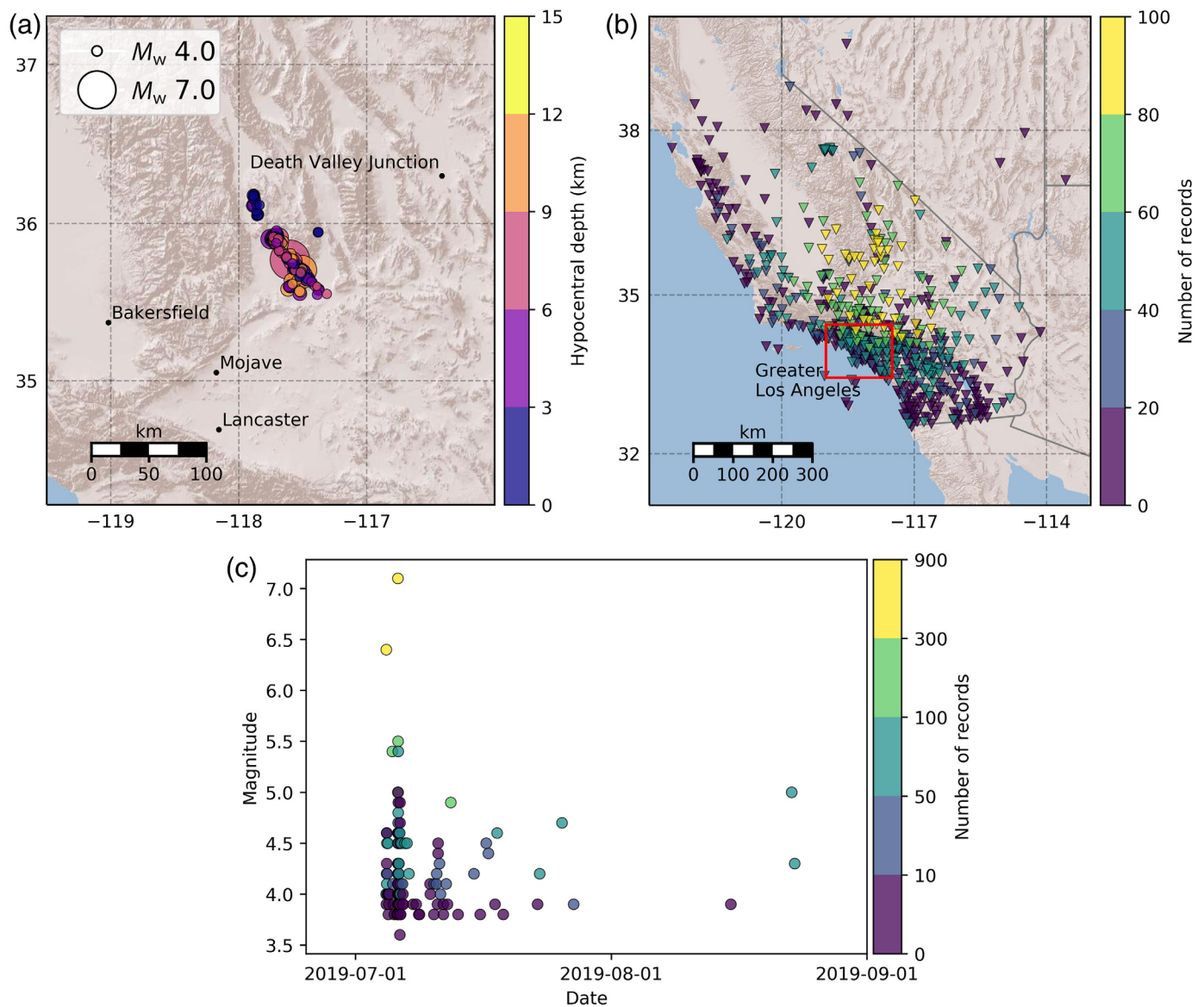
Engineering Strong Motion Data (CESMD), and the gmprocess software provides readers for file formats used by CESMD; a new webservice interface recently became available at the CESMD, but at the time of this writing, the gmprocess software does not yet provide an interface to it.

## Data Collection

We selected earthquakes by querying the USGS Comprehensive Catalog (ComCat; [Guy et al., 2015](#)) for all  $M_w$  3.8 or greater earthquakes between 1 July 2019 (UTC) and 1 September 2019, from 34.715 to 36.554 latitude and  $-118.828$  to  $-116.367$  longitude, which results in 170 events. This query reflected the data available in ComCat as of 23 August 2019. The ComCat database receives earthquake data from Advanced National Seismic System (ANSS) contributing seismic networks and relies on a set of business rules that allows it to select which information is preferred. The preferred source depends on the earthquake location; each ANSS seismic network is primarily responsible for earthquakes in their authoritative region. The SCSN is the preferred ANSS contributor for events located in southern California. Although moment magnitudes are the preferred magnitude type, they are not available for all events, and thus when we perform a ComCat query, it is matching our search criteria against a catalog of earthquake magnitudes with variable magnitude types.

Because the source information in our final data set reflects the data available in ComCat as of 13 November 2019, the range of magnitudes in our final database may appear inconsistent relative to the event selection criteria described previously. Because of the manner in which earthquake magnitudes are updated with time, some of the initially selected events no longer meet the original query criteria, and the minimum magnitude in the database is 3.6 although we have not included most events that occurred in the  $M_w$  3.6–3.8 range. ComCat archives the full history of all magnitude estimates, and this information could easily be retrieved by users of the data set (using the event IDs associated with each earthquake) to ensure that they have the most up-to-date information possible at the time of their analysis, or to select a nonpreferred earthquake origin, in which the origin refers to the earthquake time, location, and magnitude.

We obtained waveform data from the IRIS Data Management Center (DMC), the Northern California Earthquake Data Center (NCEDC; [Northern California Earthquake Data Center \[NCEDC\], 2014](#)), the Southern California Earthquake Data Center (SCEDC; [Southern California Earthquake Center \[SCEDC\], 2013](#)), and the CESMD (see [Data and Resources](#)). For the FDSN webservices (IRIS, NCEDC, SCEDC), we requested data for strong-motion stations with the time window starting 30 s before the origin time and ending 5 min after the origin time. For earthquakes with magnitude greater than or equal to 4.0, we requested data up to 350 km away from the earthquake epicenter. For earthquakes with magnitude less than 4.0, we



requested data up to 200 km away from the epicenter. Figure 1 shows a map of the earthquake locations, a map of station locations indicating the number of records at each station, and the earthquake magnitudes with time indicating the number of records per event that have passed the quality assurance checks.

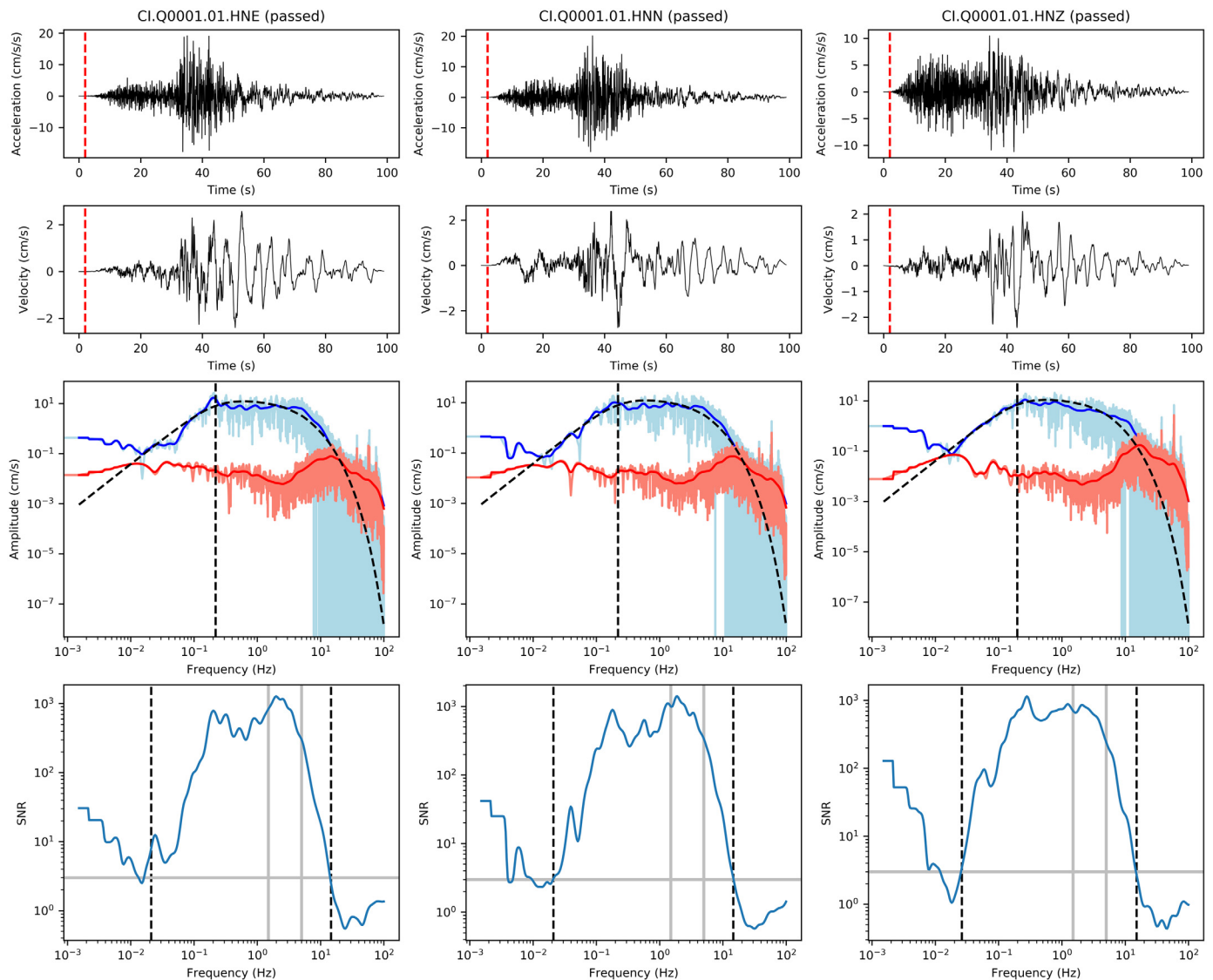
We applied the following initial quality control checks on the waveform data:

- For records that include information about the station type (e.g., the Consortium of Organizations for Strong-Motion Observation Systems format and Bureau of Reclamation data) such as free field, structural array, or geotechnical array, we remove data from any nonfree-field stations.
- We require a minimum sampling rate of 40.0 Hz; the minimum sample rate in any record that passed all checks is 100 Hz.

**Figure 1.** (a) Map of earthquakes depicting magnitude and hypocentral depth, (b) map of stations depicting the number of recordings per station, and (c) earthquake magnitude as a function of time depicting the number of recordings per event that have passed the quality control checks. The color version of this figure is available only in the electronic edition.

- We remove any stations with more than three channels for the same instrument type; this typically occurs for structural or downhole arrays.
- We require that the start times, number of points, and durations of the different channels of an instrument match; the code attempts to align the channels by first trimming the time series, and if that is not successful then it tries to resample to an aligned time series, but this algorithm can fail under degenerate circumstances.
- We require that the automatically selected noise window duration is 1 s or longer, and the signal window duration is





5 s or longer. The noise and signal windows are separated by the estimated  $P$ -wave arrival time (see Fig. 2). Additional details of how the signal and noise windows are selected are given later. Figure 2 does not display the full extent of the available time history, and the noise window is generally much longer than displayed.

- We apply a short-term average (STA) to long-term average (LTA) ratio (STA/LTA) check, in which the STA and LTA durations are 1.0 and 20 s, respectively. The maximum STA/LTA for each channel must exceed 3. We use the same window durations as [Cauzzi et al. \(2016\)](#) but a more lenient ratio threshold; this check has the side effect of requiring a minimum channel duration to be the LTA duration.
- We require a minimum of 0.1 zero crossings per second within the signal window for each channel.
- We require that the signal-to-noise ratio (SNR) exceeds 3.0 from 0.2 to 5.0 Hz for each channel (see Fig. 2). The Fourier amplitude spectra of the noise and signal windows

**Figure 2.** Summary plot of processed ground motions for station CI.Q0001 for the  $M_w$  7.1 Ridgecrest mainshock. Each column of plots is for a different channel. The top row of plots gives the acceleration record; the second row of plots gives the velocity record. The estimated  $P$ -wave arrival time is given as the red vertical dashed line in the acceleration and velocity plots. The third row of plots gives the fast Fourier transform (FFT) of the signal window (light blue) and the noise window (light red), and the smoothed FFT for the signal window (dark blue) and noise window (dark red). As a visual aid, the third row of plots also gives a Brune spectrum ([Brune, 1970, 1971](#)) fit to the smoothed signal spectra (dashed line) and the associated corner frequency (vertical dashed line). The fourth row of plots gives the signal-to-noise ratio (SNR) based on the smoothed noise and signal spectra. The vertical gray bars indicate the bandwidth for which the SNR is required to exceed the threshold (indicated by the horizontal gray bar). The selected corner frequencies for the band-pass filtering are given as the vertical dashed lines. The color version of this figure is available only in the electronic edition.

TABLE 1  
Number of Records for Each Network That Passed Quality Checks

Network Code	Name	Number of Records	Citation
CI	Southern California Seismic Network (SCSN)	15,447	California Institute of Technology and U.S. Geological Survey Pasadena (1926)
CE	California Strong Motion Instrumentation Program	1,664	See <a href="#">Data and Resources</a>
NC	Northern California Seismic Network (NCSN)	1,209	USGS Menlo Park (1967)
NP	United States National Strong-Motion Network	1,095	U.S. Geological Survey (1931)
BK	Berkeley Digital Seismic Network	858	Northern California Earthquake Data Center (NCEDC) (2014)
AZ	ANZA regional network	763	Vernon and UC San Diego (1982)
YN	San Jacinto fault zone experiment	638	Vernon and BenZion (2010)
GS	U.S. Geological Survey (USGS) Networks	199	Albuquerque Seismological Laboratory/U.S. Geological Survey (ASL/USGS) (1980)
PY	Piñon Flats observatory array	153	Vernon and UC San Diego (2014)
ZY	Portable Southern California Seismic Networks	143	Not available
NN	Nevada Seismic Network	127	University of Nevada, Reno (1971)
WR	California Division of Water Resources	124	Not available
PG	Central Coast Seismic Network, Pacific Gas and Electric Company (PG&E)	109	Not available
SN	Southern Great Basin Network	81	University of Nevada, Reno (1980)
BC	Red Sísmica del Noroeste de México	36	Centro de Investigación Científica y de Educación Superior de Ensenada (CICESE), Ensenada (1980)
SB	UC Santa Barbara Engineering Seismology Network	32	UC Santa Barbara (1989)
RE	US Bureau of Reclamation Seismic Networks	29	Not available
MX	Mexican National Seismic Network	1	Red Sísmica Mexicana, see <a href="#">Data and Resources</a>

are smoothed using the [Konno and Ohmachi \(1998\)](#) method with a smoothing parameter of 20.

- In the case in which a station had multiple strong-motion instruments, we include the instrument with the higher sampling rate and remove the other instrument.

Waveform data that failed any one of these checks are flagged as failed and are not included in the final data tables. If we detected duplicate data from the FDSN services and CESMD, we used the data from the FDSN services. Table 1 gives the number of records for each network that passed these tests.

From the waveform request, we obtained 87,528 records that match the search criteria, in which we use the term record as the group of all of the channels available for an instrument per event. Out of these records, 22,708 passed our initial quality control checks. For each record that fails, the `gmprocess` software records the reason for failure. The total number of records that failed each test is found in Table 2, along with a description for each failure reason. The most common failure reason is that the SNR criteria were not met. This is often

caused by the presence of another event in the noise window of the record. Table 2 also shows that we received numerous duplicate data, which resulted in many records being removed from our results.

## Time-Series Processing

Processing of the time-series data followed an automated workflow that is based on the automated algorithms described by [Dawood \*et al.\* \(2016\)](#) and [Rennolet \*et al.\* \(2018\)](#), which were based on the processing procedures described by [Ancheta \*et al.\* \(2014\)](#). First, we subtract the mean from the waveform and apply the instrument sensitivity (i.e., instrument gain) to convert from counts to physical units. Next, we separate the signal from the noise using the *P*-wave arrival time. The *P*-wave arrival time is determined by computing the theoretical travel time using the International Association of Seismology and the Physics of the Earth's Interior (IASPEI) 1D seismic velocity model ([Kennett and Engdahl, 1991](#)). More precise travel times could be achieved with a velocity model specific to southern California, but we found that this global velocity model was

TABLE 2  
Number of Records That Failed Each Quality Check

Failure Description	Number of Records
The signal-to-noise ratio (SNR) is below the required threshold	50,171
A significant arrival from another event occurs within the first 70.0% of the signal window	4,496
The maximum STA/LTA is below the required threshold	1,927
The zero-crossing rate is below the required threshold	1,343
An instrument is collocated with an HN instrument and the non-HN instrument has been removed	1,281
A duplicate channel code has been detected and removed	245
The SNR exceeds the threshold, but not for the entire required bandwidth	125
The length of the noise window is less than required	33
The station includes more than three channels for the same instrument type	20
Windowing of the signal and noise failed	15
The STA/LTA check could not be performed because the record length is shorter than the LTA length	5
The duration of the signal window is less than the minimum required length	1
Channel start times do not match	1

HN, high-broadband accelerometer; LTA, long-term average; STA, short-term average.

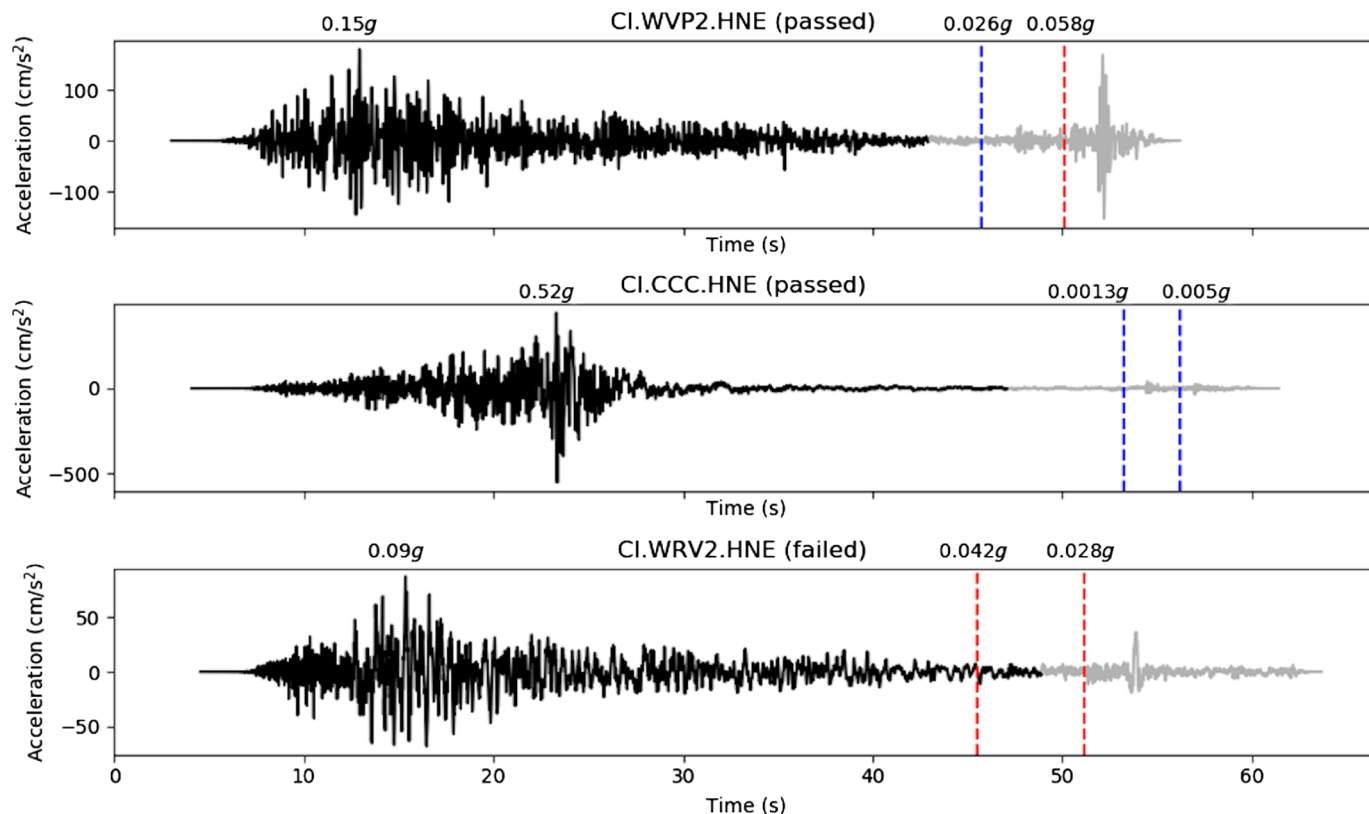
sufficiently accurate for separating the signal and noise. If the theoretical *P*-wave arrival time lies outside the time window of our waveform, then we evaluate several *P*-wave picker algorithms: Akazawa (2004), Baer and Kradolfer (1987), Kalkan (2016), and Earle and Shearer (1994). Of these algorithms, we use the *P*-wave arrival that results in the largest SNR. For the duration of the signal window, we use the mean plus two standard deviations for the 5%–95% significant duration given by Afshari and Stewart (2016). In evaluating the Afshari and Stewart (2016) duration model, we make the following conservative assumptions (in the sense that these assumptions tend to increase the duration): the time-averaged shear-wave velocity to 30 m ( $V_{30}$ ) is 180 m/s, the mechanism is normal, and the rupture distance equals the epicentral distance.

After windowing the time series, we compute the SNR as the ratio of the signal and noise spectra in the frequency domain. The noise and signal windows are each centered, tapered using a 5% Hanning taper, transformed to the frequency domain, and smoothed with the Konno and Ohmachi (1998) method with the smoothing parameter equal to 20. The high-pass and low-pass corner frequencies are chosen such that the SNR exceeds 3.0 within the passband. Relying on this SNR-based

criterion alone for selecting corner frequencies may result in a low-pass corner equal to the Nyquist frequency. To avoid this, we cap the low-pass corner frequency at 0.75 times the Nyquist frequency. We force the corner frequencies to be consistent for the horizontal components of a given instrument by selecting the minimum of the low-pass corner frequencies, and the maximum of the high-pass corner frequencies for the two horizontal channels. We then apply high-pass and low-pass filters using a five-pole, acausal Butterworth filter. Finally, we use the baseline correction method described by Ancheta *et al.* (2013), in which a sixth-order polynomial is fit to the displacement time series, in which the zero- and first-order terms are constrained to be zero. D'Amico *et al.* (2019) showed that the general approach of band-pass filtering that we currently employ cannot reliably reproduce the displacement record, and we do not intend for these records to be used for purposes in which an accurate estimate of displacement is important. Similarly, care should be taken to only use spectral periods that are within the usable bandwidth, typically defined as frequencies greater than 1.25 times the low-pass corner (Abrahamson and Silva, 1997).

After performing the time-series processing steps, we perform a final check that aims to identify records that contain signals from multiple earthquakes. This check was developed because of concerns that the intensity metrics for a record might be affected by later-arriving signals from separate earthquakes. The algorithm for performing this check is illustrated in Figure 3 and is accomplished with the following steps:

- We request an earthquake catalog from ComCat that contains all earthquakes in the region with magnitudes above 2.5. Earthquakes with magnitudes below 2.5 were not considered because it is unlikely that their signals would be significant enough to affect the records.
- For each earthquake and station pair, we compute the theoretical *P*-wave travel time using the IASPEI 1D seismic velocity model. For computational efficiency, we create a 2D grid of depths and distances that spans the range of values in the data set. We then calculate the travel time for each grid point, which we linearly interpolate to each earthquake-station pair.
- Using this table of travel-time calculations, we then identify earthquakes in which the arrival time is contained within the signal window of the record. If no arrivals are found within the signal window, then the record passes this check and the record is not modified.
- If one or more arrivals are found within the signal window, then we compute the predicted peak ground acceleration (PGA) associated with each arrival using the Boore *et al.* (2014) model. In evaluating the model for the multi-event detection algorithm, we assume that  $V_{30}$  is equal to 760 m/s and that the rupture distance is equal to the hypocentral distance. If a predicted PGA is greater than a



factor of 0.2 times the PGA of the record, then the arrival is classified as significant.

- If all of the predicted PGAs are not significant, then the record is unmodified (e.g., record CI.CCC in Fig. 3).
- If any of the significant arrivals occur within the first 70% of the signal window, then the record is rejected (e.g., record CI.WRV2 in Fig. 3).
- If all of the significant arrivals occur beyond the first 70% of the signal window, then the record is trimmed such that the record end time is equal to the arrival time of the first significant event (e.g., record CI.WVP2 in Fig. 3).

## Metrics, Metadata, and Data Format

For each record that passed processing checks, we compute various metrics, including intensity measure types (for multiple component definitions) and site metrics. The intensity measure types include PGA, peak ground velocity, pseudospectral accelerations, 5%–95% significant duration, and smoothed Fourier acceleration spectra (FAS) amplitudes. The horizontal components for the SA are combined with the orientation independent RotD50 method (Boore, 2010) for 21 oscillator periods between 0.01 and 10 s, which are the set of periods used for computing hazard curves by the NSHM (Shumway et al., 2019). The horizontal components of the FAS are combined with the quadratic mean (which is orientation independent, consistent with the computation of Kottke et al., 2018) for 80 logarithmically spaced periods between 0.02 and 10 s.

**Figure 3.** Demonstration of the multiple event detection algorithm. A single component is shown for (a–c) three different stations (CI.WVP2, CI.CCC, and CI.WRV2) that recorded the  $M_w$  7.1 mainshock. In each subplot, the peak ground acceleration (PGA) of the entire record is labeled above the time series at the time where the PGA occurs. The dashed lines indicate the arrival times from later-arriving events. For each of these arrivals, the predicted PGA is evaluated and is shown above the dashed line. If the predicted PGA is greater than 0.2 times the entire record PGA, then the arrival is deemed significant. Red, dashed lines indicate arrivals from events that are deemed significant, whereas blue, dashed lines indicate arrivals from events that are not deemed significant. For each station, the first 70% of the signal window is shown in solid black, and the remaining 30% is shown in light gray. As shown, both stations WVP2 and CCC pass because a significant event does not occur in the first 70% of the signal window. Station WRV2, however, fails the check because a significant event is found within the first 70% of the signal window. This indicates a limitation of this algorithm, as the time series for WRV2 indicates that the actual PGA for the later-arriving events is much smaller than the predicted PGA, such that the station should not have been rejected. The color version of this figure is available only in the electronic edition.

We also report the Arias intensity, combining the horizontal components with the arithmetic mean (which is orientation independent), and the 5%–95% significant duration, in which we follow the convention adopted by Afshari and Stewart (2016) of combining the horizontal components as the geometric mean.



In addition to intensity metrics, we also compute commonly used earthquake distances. These include epicentral and hypocentral distances and finite-source distances. For the two largest events (the  $M_w$  6.4 and 7.1 events), the finite-source distances are based on the rupture extent, as estimated from surface rupture detected by National Aeronautics and Space Administration Advanced Rapid Imaging and Analysis coseismic interferogram from the Advanced Land Observing Satellite 2 (Sang-Ho Yun, written comm., 2019).

Finite-source distances include the closest distance to the rupture plane ( $R_{RUP}$ ), the closest distance to the surface projection of the rupture plane (i.e., Joyner–Boore distance  $R_{JB}$ ), and the strike-parallel (T) and strike-normal (U) coordinates (Spudich and Chiou, 2015). We also include distances derived from U and T, including the distance measured perpendicular to the fault strike from the surface projection of the up-dip edge of the fault plane ( $R_X$ ), the distance measured parallel to the fault strike from the midpoint of the surface projection of the fault plane ( $R_Y$ ), and the horizontal distance off the end of the rupture measured parallel to strike ( $R_{Y0}$ ). For earthquakes without an estimated rupture extent, the finite-source distances ( $R_{RUP}$  and  $R_{JB}$ ) must be approximated, and we do so using the method described by Thompson and Worden (2017). In particular, the mean and standard deviation of the finite-source distance is computed considering the distribution of source dimensions and orientations consistent with the point-source distance and magnitude of the earthquake.

In the database, we also include multiple  $V_{S30}$  estimates. All stations have an estimate of  $V_{S30}$  from topographic slope using the Wald and Allen (2007) method, and all stations in California have an estimate using the Thompson *et al.* (2014) map, which was updated by Thompson (2018) to reflect the improved geology-based  $V_{S30}$  map by Wills *et al.* (2015). In addition, we tabulate measured  $V_{S30}$  values and the standard deviation of the measurements from the database compiled by Seyhan *et al.* (2014).

We also tabulate the source-to-site back azimuth, which has recently been useful to identify trends in ground-motion residuals that correlate with shear-wave radiation patterns (Kotha *et al.*, 2019). Many other interesting metrics would be valuable to include (e.g., strike, rake, and dip); however, we do not have methods to automatically estimate these source parameters.

We use an extension of the adaptable seismic data format (ASDF; Krischer *et al.*, 2016), which is a schema for the widely used hierarchical data format (HDF, see Data and Resources), to store the raw waveform data, event data, processed waveform data, important intermediate results, and station and waveform metrics. The layout of the ASDF format is illustrated in Figure 4. The ASDF file also contains provenance information that follows the SEIS-PROV standard (Krischer, Smith, and Tromp, 2015). The provenance information gives the details of all of the processing operations that have been performed on each of the waveforms. We include information not

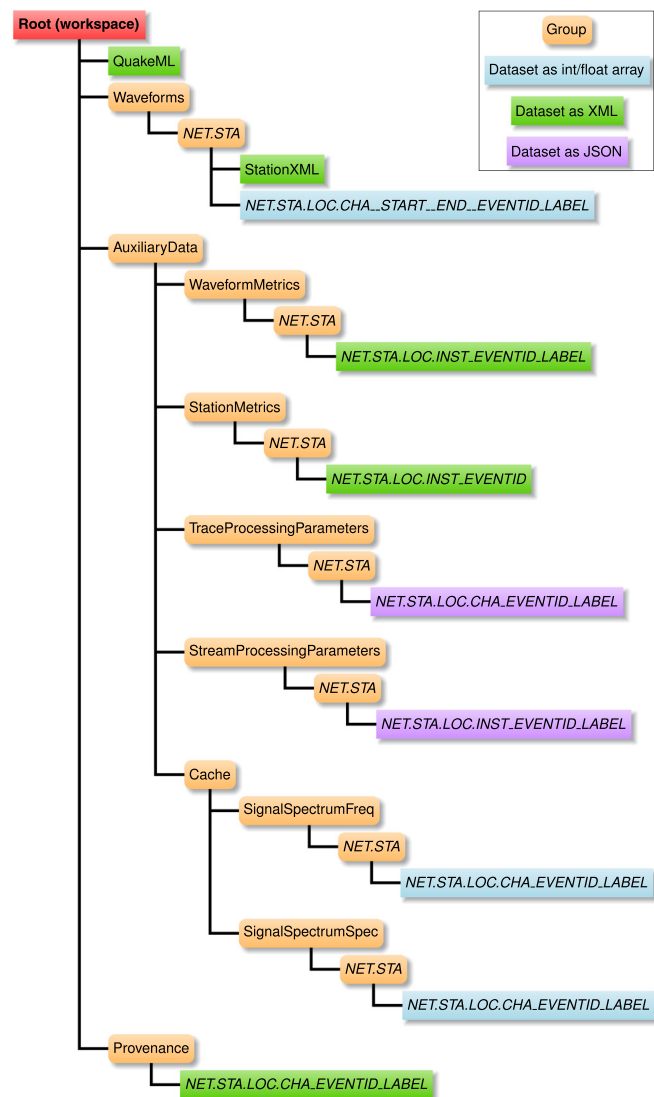
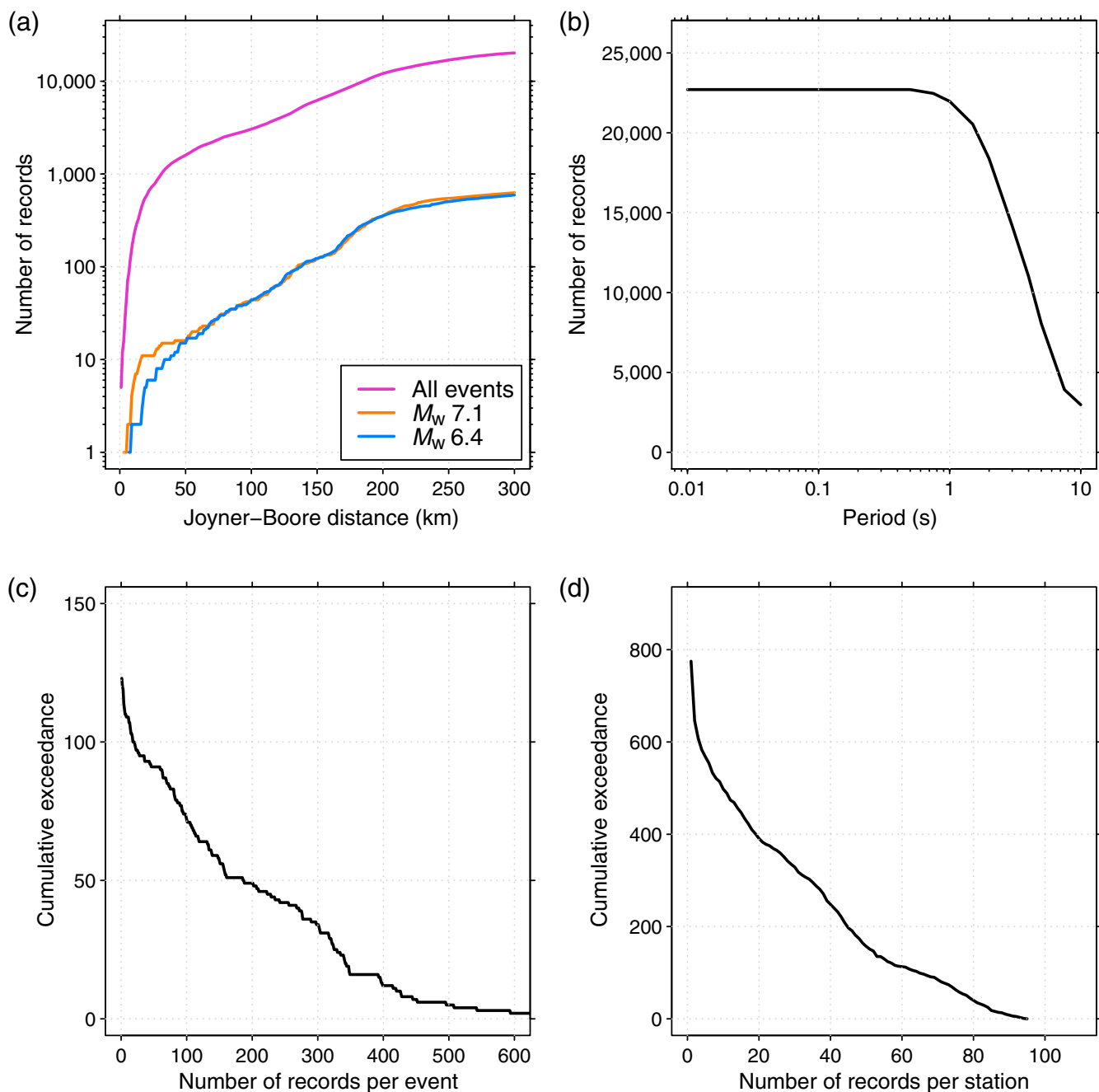


**Figure 4.** Diagram illustrating the layout of our extension of the adaptable seismic data format (ASDF) hierarchical data format5 (HDF5) format using the AuxiliaryData group. The data are grouped by station, and for brevity we only show one example per station. We create the tags based on the station and event information along with a user-specified label and make use of the following variables (shown in *italics*): NET, Federation of Digital Seismograph Networks (FDSN) network code (or equivalent); STA, station code; LOC, location code; CHA, SEED channel code (or equivalent); INST, first two letters of the channel code (dropping the third letter which corresponds to the component); START\_\_END, channel start and end timestamps for waveforms; LABEL, user-specified label that uniquely identifies processing parameters; and EVENTID, Comprehensive Catalog (ComCat) event id (or equivalent). The waveforms and spectra are stored as floating point arrays; the event, station metadata, and provenance information are stored as Extensible Markup Language (XML) encoded as bytes; and the processing parameters are stored as JSON encoded as bytes. The color version of this figure is available only in the electronic edition.





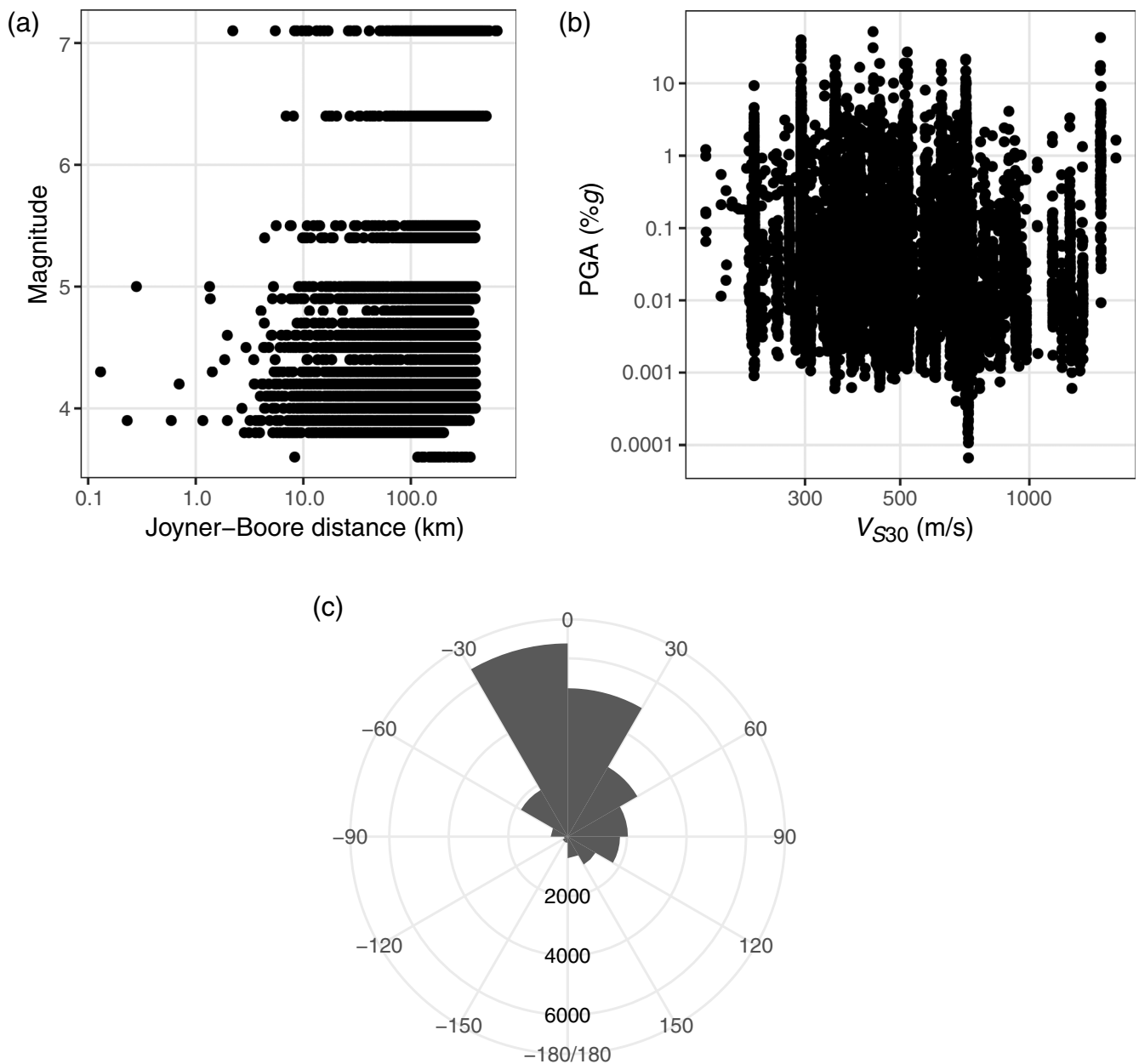
explicitly covered in the ASDF format specification in the AuxiliaryData group such as waveform metrics. We also distribute metrics and metadata in flat files for ease of use by those who do not need the level of detail provided by the ASDF files.

## Initial Observations

An important feature of this data set is the distribution of the data with respect to distance, period, event, and station (Figs. 5 and 6). Ground motions at short distances for large magnitude earthquakes are particularly important for earthquake hazards. Of the 22,708 records that passed the automated screening criteria described earlier, more than 1500 were recorded within

**Figure 5.** Summary of the number of processed records:

(a) cumulative number of stations as a function of Joyner-Boore distance; (b) number of records as a function of period, in which records are included for periods greater than the period of the low-pass filter times 1.25 and less than the period of the high-pass corner divided by 1.25; (c) the cumulative number of events with at least the number of records per event given on the horizontal axis; and (d) the cumulative number of stations with at least the number of records per station given on the horizontal axis. The color version of this figure is available only in the electronic edition.



50 km of the earthquake epicenter (Fig. 5a). The closest recording for the  $M_w$  7.1 event was at a Joyner–Boore distance of 2.2 km, with five recordings at distances less than 10 km and 11 recordings at distances less than 20 km. The closest recording for the  $M_w$  6.4 event was at 6.9 km, with two recordings at distances less than 10 km and five recordings at distances less than 20 km. The number of usable records also decreases at longer periods (Fig. 5b) due to the high-pass filtering of the records described previously. The influence of the low-pass filter on the usable frequency range is not relevant for the analysis of SA because the energy that is contributing to the SA oscillator response is controlled by frequencies smaller than the low-pass corner frequency (Douglas and Boore, 2011; Bora *et al.*, 2016), but the effects of the low-pass filter would need to be considered for the analysis of Fourier spectra.

**Figure 6.** Distribution of records with respect to (a) Joyner–Boore distance and magnitude, (b)  $V_{S30}$  and PGA, and (c) back azimuth.

For constraining repeatable source and site effects, it is of interest to know the distribution of the number of records per event and per station. There are 100 events with 20 or more records and 49 events with 200 or more records (Fig. 5c). There are 391 stations with 20 or more records and 248 stations with 40 or more records (Fig. 5d).

The joint distribution of the data with respect to some parameters is also of interest (Fig. 6). In particular, the magnitude–distance distribution illustrates that the network coverage for these events includes good coverage in large-magnitude events (Fig. 6a). The  $V_{S30}$ –PGA distribution shows that PGA

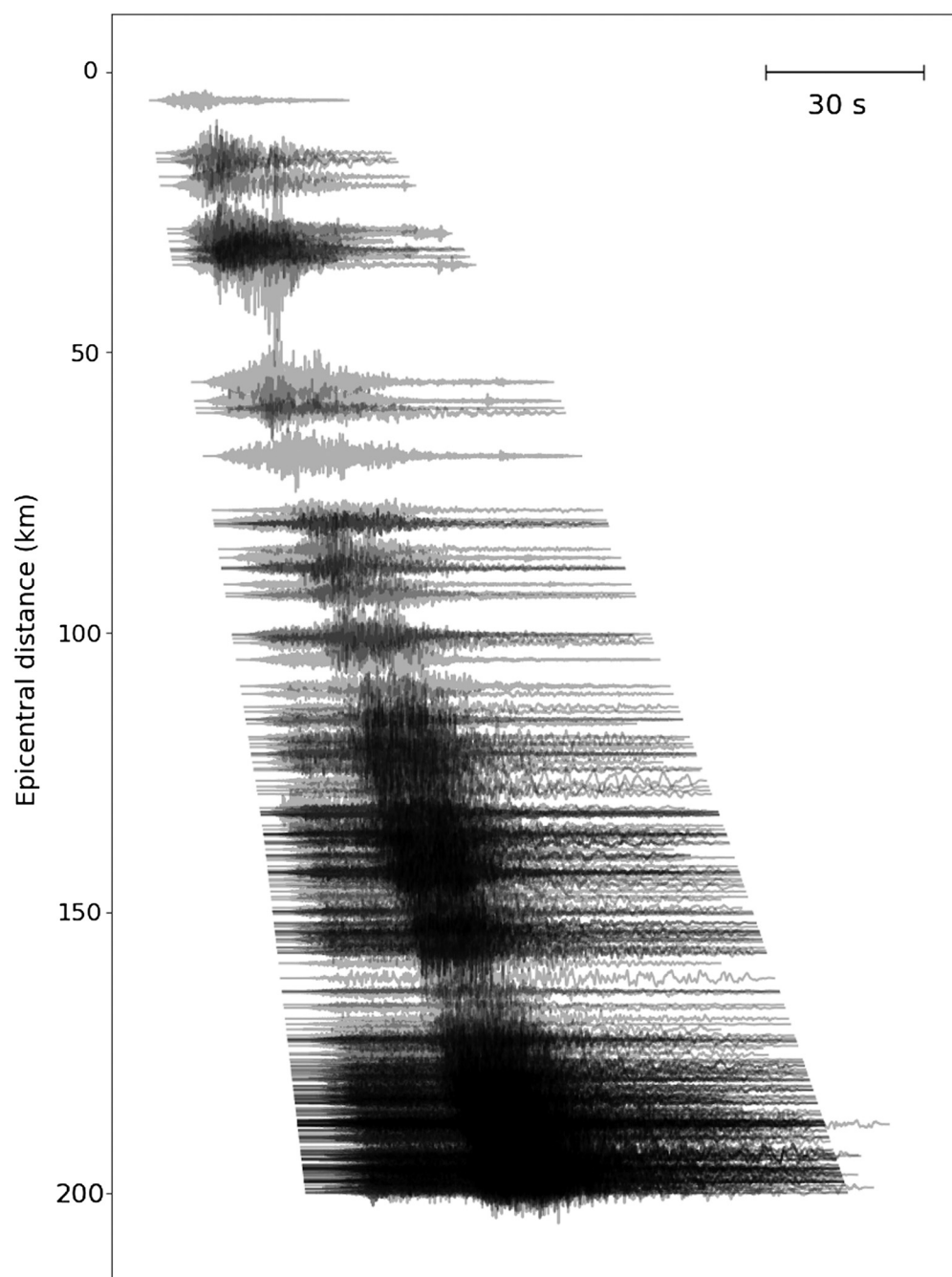


**Figure 7.** Moveout plot for all processed acceleration records (up to 200 km) from the  $M_w$  7.1 mainshock that passed quality checks. The east component is shown for all records. Each waveform has been normalized by multiplying by the epicentral distance.

exceeded the 10%g threshold where nonlinear effects are expected (Kaklamanos *et al.*, 2013) for a fairly broad range of  $V_{S30}$  values, although the minimum  $V_{S30}$  for which PGA exceeded 10%g is about 290 m/s. This value of  $V_{S30}$  is indicative of a stiff soil site and suggests that nonlinearity might not be well captured in the instrumental data. The rose diagram of back azimuths (Fig. 6c) demonstrates that the network coverage is not uniform because stations have been preferentially placed near Los Angeles, California.

tion and waveform metrics. We have described the processing methods and the resulting data set in the hope that the rapid collection and dissemination of this information will lead to more detailed analysis of this earthquake sequence.

## Data and Resources

The data compiled and processed in this article have been obtained from the Center for Engineering Strong Motion Data (CESMD; [www.strongmotioncenter.org](http://www.strongmotioncenter.org)), Southern California Earthquake Data

Record sections, or move-out plots, are useful for visually checking for potential problems with the data in the time domain (Fig. 7). This can illuminate problems in the metadata, such as the time of the start of the record, that would not be evident in the derived waveform metrics. These plots are also useful for looking for the presence of arrivals from multiple earthquakes. The record section in Figure 7 gives us confidence that the processing steps described previously are generally working as intended.

Finally, we inspect the derived waveform metrics (Fig. 8), including PGA, the 1 s FAS, 5%–95% significant duration, and Arias intensity. Each of these metrics should exhibit simple trends with magnitude and distance. Outliers in plots of these metrics are often indicative of problems in the processing (e.g., incorrect instrument gain). The plots of the waveform metrics show the general trends expected for these metrics: PGA, FAS, and Arias intensity all decrease with distance and increase with magnitude, whereas significant duration increases with distance and magnitude.

## Summary

Our effort herein to quickly process the ground-motion data from the 2019 Ridgecrest, California, earthquake sequence includes the compilation of sta-

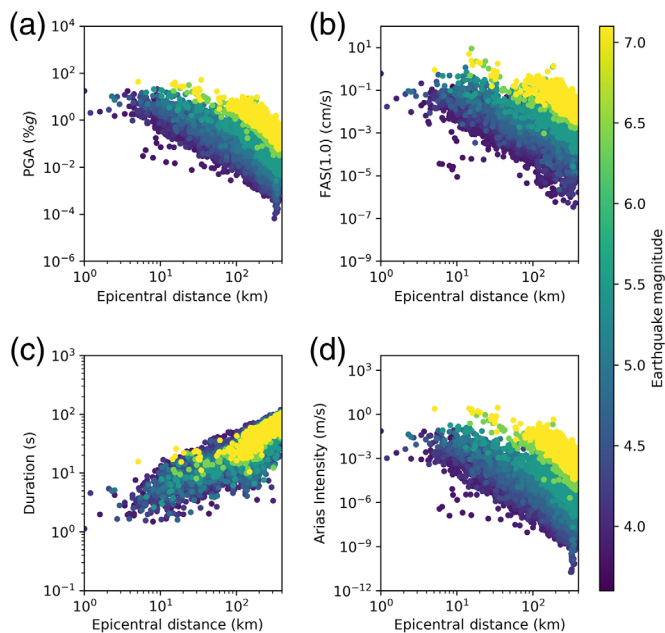


**Figure 8.** Intensity measures scaling with distance, colored by magnitude for (a) PGA, (b) smoothed Fourier amplitude, (c) 5%–95% significant duration, and (d) Arias intensity. FAS, Fourier acceleration spectra. The color version of this figure is available only in the electronic edition.

Center (SCEDC; [SCEDC, 2013](#)), the Northern California Earthquake Data Center (NCEDC; [NCEDC, 2014](#)), Red Sísmica Mexicana (n.d.). doi: [10.21766/ssnm/sn/mx](#), and the Incorporated Research Institutions for Seismology (IRIS). The facilities of IRIS Data Services, and specifically the IRIS Data Management Center (DMC), were used for access to waveforms, related metadata, and/or derived products used in this study. IRIS Data Services is funded through the Seismological Facilities for the Advancement of Geoscience and EarthScope (SAGE) Proposal of the National Science Foundation (NSF) under Cooperative Agreement EAR-1261681. The open-source software used for processing the data is version 1.0 of [Hearne et al. \(2019\)](#). The adaptable seismic data format (ASDF) files containing the raw and processed waveforms, the derived intensity metrics, and the metadata are available from [Rekoske et al. \(2019\)](#). The SeisComp3 software is available at <https://www.seiscomp3.org>. Hierarchical data format is available at <https://www.hdfgroup.org>. California Strong Motion Instrumentation Program is available at <https://www.conservation.ca.gov/cgs/smip>. All websites were last accessed in November 2019.

## Acknowledgments

The authors thank Carlo Cauzzi, Sreeram Reddy Kotha, Dan McNamara, and Janet Slate for their valuable reviews of this article. Development of the gmprocess software was partially funded by The Pacific Gas and Electric Company (PG&E) through a Collaborative Research and Development Agreement.

## References

Abrahamson, N. A., and W. J. Silva (1997). Empirical response spectral attenuation relations for shallow crustal earthquakes, *Seismol. Res. Lett.* **68**, 94–127.

- Afshari, K., and J. P. Stewart (2016). Physically parameterized prediction equations for significant duration in active crustal regions, *Earthq. Spectra* **32**, 2057–2081.
- Akazawa, T. (2004). A technique for automatic detection of onset time of P- and S-phases in strong motion records, *Proc. of the 13th World Conf. on Earthquake Engineering*, Vancouver, Canada, 1–6 August 2004.
- Akkar, S., M. A. Sandikkaya, M. Şenyurt, A. Azari Sisi, B. Ö. Ay, P. Traversa, J. Douglas, F. Cotton, L. Luzi, B. Hernandez, and S. Godey (2014). Reference database for seismic ground-motion in Europe (RESORCE), *Bull. Earthq. Eng.* **12**, 311–339, doi: [10.1007/s10518-013-9506-8](#).
- Albuquerque Seismological Laboratory/U.S. Geological Survey (ASL/USGS) (1980). U.S. Geological Survey Networks, *International Federation of Digital Seismograph Networks, Dataset/Seismic Network*, doi: [10.7914/SN/GS](#).
- Ancheta, T. D., R. B. Darragh, J. P. Stewart, E. Seyhan, W. J. Silva, B. S. J. Chiou, K. Wooddell, R. W. Graves, A. R. Kottke, D. M. Boore, and T. Kishida (2013). *PEER NGA-West2 Database*, Pacific Earthquake Engineering Research (PEER) Center, University of California, Berkeley, Berkeley, California.
- Ancheta, T. D., R. B. Darragh, J. P. Stewart, E. Seyhan, W. J. Silva, B. S. J. Chiou, K. E. Wooddell, R. W. Graves, A. R. Kottke, D. M. Boore, and T. Kishida (2014). NGA-West2 database, *Earthq. Spectra* **30**, 989–1005.
- Baer, M., and U. Kradolfer (1987). An automatic phase picker for local and teleseismic events, *Bull. Seismol. Soc. Am.* **77**, 1437–1445.
- Bindi, D., S. R. Kotha, G. Weatherill, G. Lanzano, L. Luzi, and F. Cotton (2019). The pan-European engineering strong motion (ESM) flatfile: Consistency check via residual analysis, *Bull. Earthq. Eng.* **17**, 583–602.
- Boore, D. M. (2010). Orientation-independent, nongeometric-mean measures of seismic intensity from two horizontal components of motion, *Bull. Seismol. Soc. Am.* **100**, 1830–1835.
- Boore, D. M., J. P. Stewart, E. Seyhan, and G. M. Atkinson (2014). NGA-West2 equations for predicting PGA, PGV, and 5% damped PSA for shallow crustal earthquakes, *Earthq. Spectra* **30**, 1057–1085.
- Bora, S. S., F. Scherbaum, N. Kuehn, and P. Stafford (2016). On the relationship between Fourier and response spectra: Implications for the adjustment of empirical ground-motion prediction equations (GMPEs), *Bull. Seismol. Soc. Am.* **106**, 1235–1253.
- Brune, J. N. (1970). Tectonic stress and the spectra of seismic shear waves from earthquakes, *J. Geophys. Res.* **75**, 4997–5009.
- Brune, J. N. (1971). Correction, *J. Geophys. Res.* **76**, 5002.
- California Institute of Technology and U.S. Geological Survey Pasadena (1926). Southern California Seismic Network, *International Federation of Digital Seismograph Networks, Dataset/Seismic Network*, doi: [10.7914/SN/CI](#).
- Cauzzi, C., R. Sleeman, J. Clinton, J. D. Ballesta, O. Galanis, and P. Kästli (2016). Introducing the European rapid raw strong-motion database, *Seismol. Res. Lett.* **87**, 977–986.
- Centro de Investigación Científica y de Educación Superior de Ensenada (CICESE), Ensenada (1980). Red Sísmica del Noroeste de México, *International Federation of Digital Seismograph Networks, Dataset/Seismic Network*, doi: [10.7914/SN/BC](#).
- Chiou, B., R. Darragh, N. Gregor, and W. Silva (2008). NGA project strong-motion database, *Earthq. Spectra* **24**, 23–44.



- Cochran, E. S., E. Wolin, D. E. McNamara, A. Yong, D. Wilson, M. Alvarez, N. van der Elst, and A. McClain (2019). The U.S. Geological Survey's rapid seismic array deployment for the 2019 Ridgecrest earthquake sequence, *Seismol. Res. Lett.*, doi: [10.1785/0220190296](https://doi.org/10.1785/0220190296).
- D'Amico, M., C. Felicetta, E. Schiappapietra, F. Pacor, F. Gallovič, R. Paolucci, R. Puglia, G. Lanzano, S. Sgobba, and L. Luzi (2019). Fling effects from near-source strong-motion records: Insights from the 2016 Mw 6.5 Norcia, Central Italy, *Seismol. Res. Lett.* doi: [10.1785/0220180169](https://doi.org/10.1785/0220180169).
- Dawood, H. M., A. Rodriguez-Marek, J. Bayless, C. Goulet, and E. Thompson (2016). A flatfile for the KiK-net database processed using an automated protocol, *Earthq. Spectra* **32**, 1281–1302.
- Douglas, J., and D. M. Boore (2011). High-frequency filtering of strong-motion records, *Bull. Earthq. Eng.* **9**, 395–409.
- Earle, P. S., and P. M. Shearer (1994). Characterization of global seismograms using an automatic-picking algorithm, *Bull. Seismol. Soc. Am.* **84**, 366–376.
- García, D., R. T. Mah, K. L. Johnson, M. G. Hearne, K. D. Marano, K. W. Lin, D. J. Wald, C. B. Worden, and E. So (2012). ShakeMap Atlas 2.0: An improved suite of recent historical earthquake ShakeMaps for global hazard analyses and loss model calibration, *World Conf. on Earthquake Engineering*, Lisbon, Portugal, 24–28 September 2012.
- García, D., D. J. Wald, and M. G. Hearne (2012). A global earthquake discrimination scheme to optimize ground-motion prediction equation selection, *Bull. Seismol. Soc. Am.* **102**, 185–203.
- Gregor, N., N. A. Abrahamson, G. M. Atkinson, D. M. Boore, Y. Bozorgnia, K. W. Campbell, B. S. J. Chiou, I. M. Idriss, R. Kamai, E. Seyhan, and W. Silva (2014). Comparison of NGA-West2 GMPEs, *Earthq. Spectra* **30**, 1179–1197.
- Guy, M. R., J. M. Patton, J. Fee, M. Hearne, E. Martinez, D. Ketchum, C. Worden, V. Quitoriano, E. Hunter, G. Smoczyk, and S. Schwarz (2015). National Earthquake Information Center systems overview and integration, *U.S. Geol. Surv. Open-File Rept. 2015-1120*, doi: [10.3133/ofr20151120](https://doi.org/10.3133/ofr20151120).
- Hearne, M., E. M. Thompson, H. Schovanec, J. Rekoske, B. T. Aagaard, and C. B. Worden (2019). USGS automated ground motion processing software, *USGS Software Release*, doi: [10.5066/P9ANQXN3](https://doi.org/10.5066/P9ANQXN3).
- Jones, J., E. Kalkan, and C. Stephens (2017). Processing and review interface for strong motion data (PRISM)—Methodology and automated processing, *U.S. Geol. Surv. Open-File Rept. 2017-1008*, 81 pp., doi: [10.3133/ofr20171008](https://doi.org/10.3133/ofr20171008).
- Kaklamanos, J., B. A. Bradley, E. M. Thompson, and L. G. Baise (2013). Critical parameters affecting bias and variability in site-response analyses using KiK-net downhole array data, *Bull. Seismol. Soc. Am.* **103**, 1733–1749.
- Kalkan, E. (2016). An automatic P-phase arrival-time picker, *Bull. Seismol. Soc. Am.* **106**, 971–986.
- Kennett, B. L. N., and E. R. Engdahl (1991). Traveltimes for global earthquake location and phase identification, *Geophys. J. Int.* **105**, 429–465.
- Konno, K., and T. Ohmachi (1998). Ground-motion characteristics estimated from spectral ratio between horizontal and vertical components of microtremor, *Bull. Seismol. Soc. Am.* **88**, 228–241.
- Kotha, S. R., F. Cotton, and D. Bindi (2019). Empirical models of shear-wave radiation pattern derived from large datasets of ground-shaking observations, *Sci. Rep.* **9**, doi: [10.1038/s41598-018-37524-4](https://doi.org/10.1038/s41598-018-37524-4).
- Kottke, A., E. Rathje, D. M. Boore, E. Thompson, J. Hollenback, N. Kuehn, C. A. Goulet, N. A. Abrahamson, Y. Bozorgnia, and A. Der Kiureghian (2018). Selection of random vibration procedures for the NGA East project, *PEER Rept. No. 2018/05*, 1–61, available at [https://peer.berkeley.edu/sites/default/files/2018\\_05\\_goulet\\_final\\_final.pdf](https://peer.berkeley.edu/sites/default/files/2018_05_goulet_final_final.pdf) (last accessed November 2019).
- Krischer, L., T. Megies, R. Barsch, M. Beyreuther, T. Lecocq, C. Caudron, and J. Wassermann (2015). Obspy: A bridge for seismology into the scientific python ecosystem, *Comput. Sci. Discov.* **8**, 1–17, doi: [10.1088/1749-4699/8/1/014003](https://doi.org/10.1088/1749-4699/8/1/014003).
- Krischer, L., J. Smith, W. Lei, M. Lefebvre, Y. Ruan, E. Sales de Andrade, N. Podhorszki, E. Bozdog, and J. Tromp (2016). An adaptable seismic data format, *Geophys. J. Int.* **207**, 1003–1011, doi: [10.1093/gji/ggw319](https://doi.org/10.1093/gji/ggw319).
- Krischer, L., J. A. Smith, and J. Tromp (2015). SEIS-PROV: Practical provenance for seismological data, *AGU Fall Meeting Abstracts*, San Francisco, California, 14–18 December 2015.
- Lanzano, G., S. Sgobba, L. Luzi, R. Puglia, F. Pacor, C. Felicetta, M. D'Amico, F. Cotton, and D. Bindi (2019). The pan-European engineering strong motion (ESM) flatfile: Compilation criteria and data statistics, *Bull. Earthq. Eng.* **17**, 561–582.
- Luzi, L., R. Puglia, E. Russo, M. D'Amico, C. Felicetta, F. Pacor, G. Lanzano, U. Ceken, J. Clinton, G. Costa, *et al.* (2016). The engineering strong motion database: A platform to access pan-European accelerometric data, *Seismol. Res. Lett.* **87**, 987–997, doi: [10.1785/0220150278](https://doi.org/10.1785/0220150278).
- McNamara, D. E., M. D. Petersen, E. M. Thompson, P. M. Powers, A. M. Shumway, S. M. Hoover, M. P. Moschetti, and E. Wolin (2018). Evaluation of ground-motion models for USGS seismic hazard forecasts: Induced and tectonic earthquakes in the central and eastern United States, *Bull. Seismol. Soc. Am.* **109**, 322–335.
- McNamara, D. E., E. Wolin, P. M. Powers, A. M. Shumway, M. P. Moschetti, J. Rekoske, E. M. Thompson, C. S. Mueller, and M. D. Petersen (2019). Evaluation of ground-motion models for U.S. Geological Survey seismic hazard models: 2018 Anchorage, Alaska, Mw 7.1 subduction zone earthquake sequence, *Seismol. Res. Lett.* doi: [10.1785/0220190188](https://doi.org/10.1785/0220190188).
- Moschetti, M. P., E. M. Thompson, J. Rekoske, M. G. Hearne, P. M. Powers, and C. Tape (2019). Ground-Motion amplification in Cook Inlet Region, Alaska, from intermediate-depth earthquakes, including the 2018 Mw 7.1 Anchorage earthquake, *Seismol. Res. Lett.* **91**, 142–152, doi: [10.1785/0220190179](https://doi.org/10.1785/0220190179).
- Northern California Earthquake Data Center (NCEDC) (2014). Northern California Earthquake Data Center, *UC Berkeley Seismological Laboratory, Dataset*, doi: [10.7932/NCEDC](https://doi.org/10.7932/NCEDC).
- Petersen, M. D., M. P. Moschetti, P. M. Powers, C. S. Mueller, K. M. Haller, A. D. Frankel, Y. Zeng, S. Rezaeian, S. C. Harmsen, O. S. Boyd, and N. Field (2015). The 2014 United States national seismic hazard model, *Earthq. Spectra* **31**, S1–S30.
- Puglia, R., E. Russo, L. Luzi, M. D'Amico, C. Felicetta, F. Pacor, and G. Lanzano (2018). Strong motion processing service: A tool to access and analyse earthquakes strong motion waveforms, *Bull. Earthq. Eng.* **16**, 2641–2651.
- Rekoske, J., E. M. Thompson, M. P. Moschetti, M. Hearne, B. T. Aagaard, and G. A. Parker (2019). Ground motions from the 2019 Ridgecrest,

- California, earthquake sequence, Center for Engineering Strong Motion Data (CESMD), doi: [10.5066/P9REBW60](https://doi.org/10.5066/P9REBW60).
- Rennolet, S. B., M. P. Moschetti, E. M. Thompson, and W. L. Yeck (2018). A flatfile of ground motion intensity measurements from induced earthquakes in Oklahoma and Kansas, *Earthq. Spectra* **34**, 1–20.
- Southern California Earthquake Center (SCEDC) (2013). Southern California Earthquake Center, *Caltech, Dataset*, doi: [10.7909/C3WD3xH1](https://doi.org/10.7909/C3WD3xH1).
- Seyhan, E., J. P. Stewart, T. D. Ancheta, R. B. Darragh, and R. W. Graves (2014). NGA-West2 site database, *Earthq. Spectra* **30**, 1007–1024.
- Shumway, A. M., B. S. Clayton, and K. S. Rukstales (2019). Data release for additional period and site class data for the 2018 National Seismic Hazard Model for the conterminous United States, *U.S. Geol. Surv. Data Release*, doi: [10.5066/P9RQMREV](https://doi.org/10.5066/P9RQMREV).
- Spudich, P. A., and B. Chiou (2015). Strike-parallel and strike-normal coordinate system around geometrically complicated rupture traces: Use by NGA-West2 and further improvements, *U.S. Geol. Surv. Open-File Rept. 2015-1028*, doi: [10.3133/ofr20151028](https://doi.org/10.3133/ofr20151028).
- Thompson, E. M. (2018). An updated Vs30 map for California with geologic and topographic constraints, *U.S. Geol. Surv. Data Release*, doi: [10.5066/F7JQ108S](https://doi.org/10.5066/F7JQ108S).
- Thompson, E. M., and C. B. Worden (2017). Estimating rupture distances without a rupture, *Bull. Seismol. Soc. Am.* **108**, 371–379.
- Thompson, E. M., D. J. Wald, and C. B. Worden (2014). A Vs30 map for California with geologic and topographic constraints, *Bull. Seismol. Soc. Am.* **104**, 2313–2321.
- UC Santa Barbara (1989). UC Santa Barbara engineering seismology network, *International Federation of Digital Seismograph Networks, Dataset/Seismic Network*, doi: [10.7914/SN/SB](https://doi.org/10.7914/SN/SB).
- University of Nevada, Reno (1971). Nevada seismic network, *International Federation of Digital Seismograph Networks, Dataset/Seismic Network*, doi: [10.7914/SN/NN](https://doi.org/10.7914/SN/NN).
- University of Nevada, Reno (1980). Southern Great Basin network, *International Federation of Digital Seismograph Networks, Dataset/Seismic Network*, doi: [10.7914/SN/SN](https://doi.org/10.7914/SN/SN).
- U.S. Geological Survey (1931). United States National Strong-Motion network, *International Federation of Digital Seismograph Networks, Dataset/Seismic Network*, doi: [10.7914/SN/NP](https://doi.org/10.7914/SN/NP).
- USGS Menlo Park (1967). USGS Northern California network, *International Federation of Digital Seismograph Networks, Dataset/Seismic Network*, doi: [10.7914/SN/NC](https://doi.org/10.7914/SN/NC).
- Vernon, F., and Y. BenZion (2010). San Jacinto fault zone experiment, *International Federation of Digital Seismograph Networks, Dataset/Seismic Network*, doi: [10.7914/SN/YN\\_2010](https://doi.org/10.7914/SN/YN_2010).
- Vernon, F., and UC San Diego (1982). ANZA regional network, *International Federation of Digital Seismograph Networks, Dataset/Seismic Network*, doi: [10.7914/SN/AZ](https://doi.org/10.7914/SN/AZ).
- Vernon, F., and UC San Diego (2014). Piñon Flats observatory array, *International Federation of Digital Seismograph Networks, Dataset/Seismic Network*, doi: [10.7914/SN/PY](https://doi.org/10.7914/SN/PY).
- Wald, D. J., and T. I. Allen (2007). Topographic slope as a proxy for seismic site conditions and amplification, *Bull. Seismol. Soc. Am.* **97**, 1379–1395.
- Wills, C. J., C. I. Gutierrez, F. G. Perez, and D. M. Branum (2015). A next generation Vs30 map for California based on geology and topography, *Bull. Seismol. Soc. Am.* **105**, 3083–3091, doi: [10.1785/0120150105](https://doi.org/10.1785/0120150105).
- Worden, C. B., and D. J. Wald (2016). ShakeMap documentation, *U.S. Geol. Surv.*, available at <https://usgs.github.io/shakemap/> (last accessed July 2019).
- Zaccarelli, R., D. Bindi, A. Strollo, J. Quinteros, and F. Cotton (2019). Stream2segment: An open-source tool for downloading, processing, and visualizing massive event-based seismic waveform datasets, *Seismol. Res. Lett.* doi: [10.1785/0220180314](https://doi.org/10.1785/0220180314).

---

Manuscript received 1 October 2019

Published online 12 February 2020